

Ultralong-range exciton transport in submillimeter-scale spherulite film of π -conjugated polymers

Received: 20 November 2024

Accepted: 13 January 2026

Published online: 28 January 2026

Check for updates

Lili Sun^{1,2}, Yong Yuan³, Yang Xu⁴, Chuanxin Wei⁵, Mingjian Ni¹, Zhiqiang Zhuo¹, Yingying Zheng¹, Xilai Jia⁶, Jiangli Cai¹, Xiang An¹, Jingmin Wang¹, Yahui Zhang¹, Qiang Zhao⁵, Yamin Han¹, Bin Liu¹, Hong-Hua Fang³, Chunfeng Zhang⁶, Chen Sun⁷, Man Xu⁵, Lubing Bai¹, Jianming Zhang⁸, Jinyi Lin^{1,8} & Wei Huang^{1,2,5}

Long-range exciton transport in organic semiconductors is essential for the performance of optoelectronic devices. However, solution-processed π -conjugated polymers films typically exhibit short exciton diffusion lengths (<20 nm) due to local imperfections or variations in interchain packing. Here, large-area submillimeter-scale spherulites are achieved by treating the spin-coated polydiarylfuorene film under solvent vapor annealing. The exciton diffusion length, visualized using transient photoluminescence microscopy, is determined to be an average of 186 nm, with a corresponding diffusion coefficient of $0.14 \text{ cm}^2 \text{ s}^{-1}$. Notably, the maximum value of exciton diffusion lengths and diffusion coefficient can reach up to approximately 396 nm and $0.63 \text{ cm}^2 \text{ s}^{-1}$, respectively. Well-ordered hierarchical structure with an outstanding chain alignment in spherulite provides a uniform excitonic energy landscape, enabling ultralong exciton diffusion. The reduced defect density in the spherulite film may result in shallower trap states, facilitating exciton diffusion and radiative recombination. Polymer light-emitting diodes based on submillimeter-scale spherulite films exhibit deep-blue electroluminescence with high brightness (4897 cd m^{-2}) at low current density and good color purity. These findings demonstrate that the long-range ordered spherulite structure can significantly enhance the excitons transport and improve the overall optoelectronic property.

Long-range transport of excitons in semiconducting polymer films is highly desirable for solution-processed optoelectronic devices. However, due to the local energetic disorder, imperfection and structural variation, most of the semiconducting polymer films present an extremely short singlet exciton diffusion length (L_D) of $5\text{--}20 \text{ nm}^{1-3}$. This is significantly shorter than the length (>100 nm) typically observed in single crystals and self-assembled nanostructures, which possess substantial intermolecular electronic coupling and π - π

stacking¹⁻⁸. For instance, single nanofibers from amphiphilic conjugated polymers (oligomer) with well-defined structures, prepared by living crystallization-driven self-assembly, yield efficient exciton diffusion with coefficients ranging from 0.5 to $1.1 \text{ cm}^2 \text{ s}^{-1}$ and L_D exceeding $200 \text{ nm}^{6,7}$. However, the complex and precise multi-step preparation of these nanostructures limits their practical applications, and obtaining well-ordered chain alignment in semiconducting polymer films for industrial-scale fabrication remains a significant challenging.

A full list of affiliations appears at the end of the paper. ✉ e-mail: sunchen@gbu.edu.cn; iamlbbai@njtech.edu.cn; iamjylin@njtech.edu.cn; vc@nwpu.edu.cn

Approaches for constructing well-ordered hierarchical structures, including delicate side-chain engineering and exquisite control of fluid flow during solution coating, have been extensively exploited in organic solar cells and organic field-effect transistors. Regarding polymer light-emitting diodes (PLEDs), a solution-processed emissive layer with a long-range-ordered intermolecular arrangement is essential for improving their efficiency, but is rarely reported, and the impact of structural order and exciton diffusion on optoelectronic performance needs systematic exploration^{9–11}.

As promising candidates for PLEDs, light-emitting π -conjugated polymers (π CPs) are easily solution-processed capacity to manufacture large-area films for solid-state optoelectronic applications^{12–15}. Nevertheless, amorphous films with disordered polymer chain arrangement generally exhibit ubiquitous exciton traps in the form of low-energy defect structures, resulting in severe non-radiative recombination and short-range localization of excitons, which could reduce the photoluminescence quantum efficiency and device performance¹⁰. Recently, crystalline organic semiconductors attracted more attentions, as their long-range ordered molecular packing facilitates both charge carrier mobility and the alignment of transition dipole moments⁶. From this perspective, transforming the conjugated polymer film with interpenetrating and entangled polymer chains into

highly crystalline self-assembled nanostructures would theoretically benefit efficient exciton diffusion and light emission properties. However, this approach still faces enormous challenges, due to the presence of ubiquitous structural defects, disorder aggregation and micro-scale grain boundaries¹⁷. The performance of high-quality light-emitting devices largely depends on the ability to fabricate ordered crystalline π CPs films that enable long-range exciton transport and diffusion.

Spherulite is the most common characteristic form of large-scale crystallized polymer, typically consisting of fibrillar crystals that grow radially and branch irregularly¹⁸, which plays significant roles in material molding and processing, especially for optical materials^{19,20}. Herein, under solvent vapor annealing (SVA) approach, large-area and continuous submillimeter-scale spherulite films were easily obtained from spin-coated films of wide bandgap polydiarylfuorene whose side chains were modified by branched 2-ethylhexyl (poly [4-(isooctyl)-9,9-diphenylfluorene-2,7-diyl]-co-[5-(isooctyl)-9,9-diphenylfluorene-2,7-diyl]), named as PEODPF (Fig. 1a). The crystalline film with multi-scale ordering and alignment of polymer chains can effectively suppress the internal defect that potentially acted as exciton traps, rendering the film an ultralong singlet-excitons diffusion length up to ~396 nm and a large diffusion coefficient (D) of $-0.63 \text{ cm}^2 \text{ s}^{-1}$. This submillimeter-scale

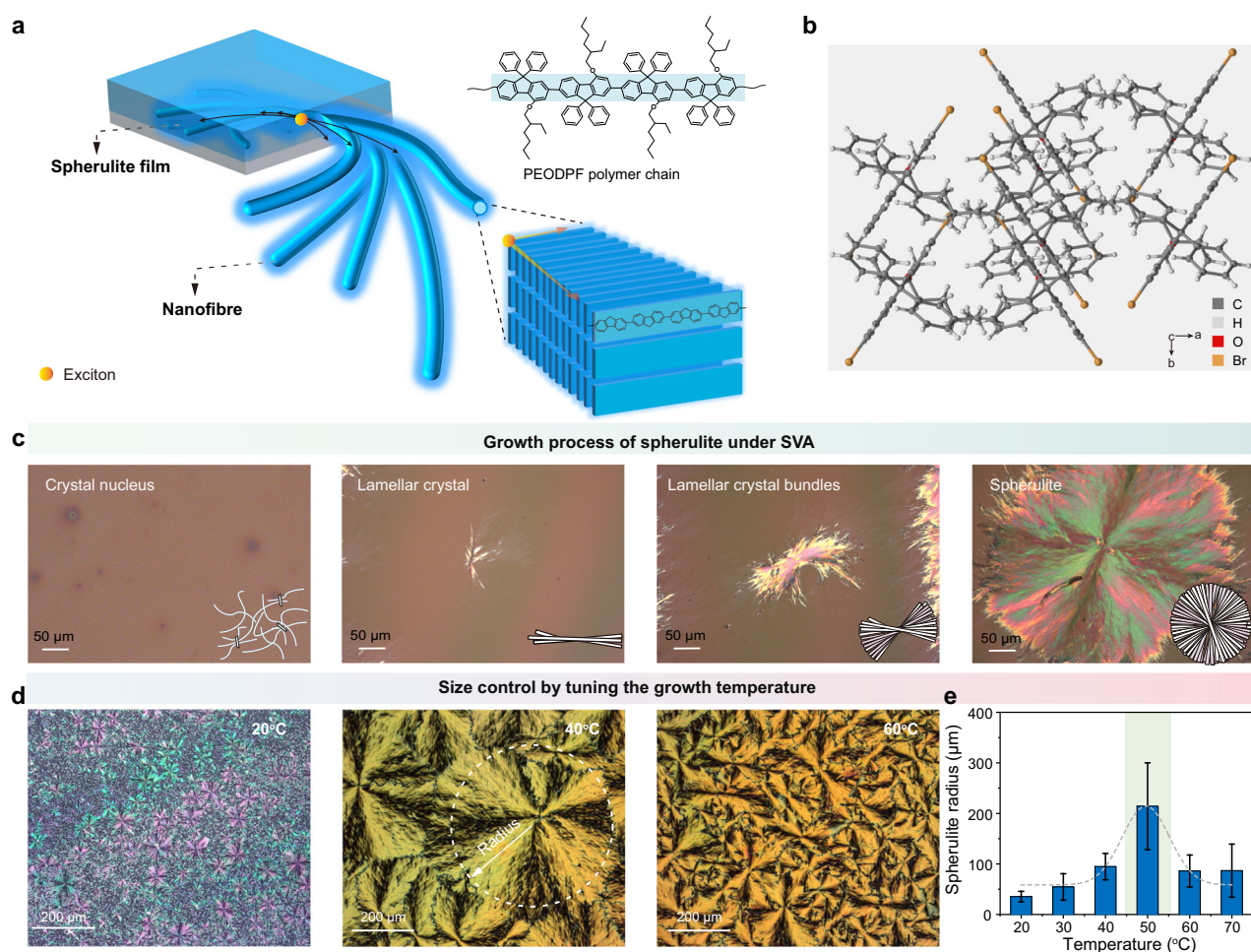


Fig. 1 | Formation mechanism of submillimeter-scale spherulite film. **a** A 3D schematic of the desired morphology composed of submillimeter-scale spherulite film based on light-emitting π -conjugated polymers to achieve ultralong-range exciton diffusion, together with the chemical structure of PEODPF. **b** Single-crystal structure of PEODPF monomer (a -axis direction). **c** Polarization microscope (POM) images of PEODPF spherulite at different growth stages together with a schematic illustration of the proposed growth model (bottom right corner). **d** Spherulite

obtained under solvent vapor annealing (SVA) processing at different environmental temperatures. **e** Histogram of radius distribution of spherulites. Data were presented as mean values \pm s.d., $n = 42$ (20 $^{\circ}\text{C}$), 30 (30 $^{\circ}\text{C}$), 26 (40 $^{\circ}\text{C}$), 9 (50 $^{\circ}\text{C}$), 26 (60 $^{\circ}\text{C}$), and 43 (70 $^{\circ}\text{C}$). Here, n denotes the number of independent spherulites identified within microscopy images acquired at the same scale for each temperature condition.

spherulite presents a deep-blue emission with high-quality color purity, which confirmed their uniform exciton energetic landscape for the potential optoelectronic application.

Results

Growth condition of spherulite

The condensed structure of π CPs in the film state is closely related to the type of side chains. As previously reported, linear side chains at the fourth position of polydiarylfuorene (PODPF) endow the polymer with exceptional backbone planarity (β -conformation), in which the intermonomer torsion angle approaches 180° , facilitating the film with unique photophysical properties and excellent crystallinity^{21,22}. Herein, the linear side chains of PODPF were replaced by branched side chains to synthesize a series of polymers, named POYDPF, PDODPF, and PEODPF, aiming to minimize aggregation in condensed states and side-chain interdigitation, as well as generating a “flexible random” region during crystallization under SVA (Fig. 1a and Supplementary Fig. 5b). As expected, only crystalline regions but no spherulitic structures were observed in PODPF film (Supplementary Fig. 5a, i), which can be attributed to the strong crystallinity of its linear alkyl chains. Interestingly, POYDPF (Supplementary Fig. 5a, ii) and PDODPF (Supplementary Fig. 5a, iii) with shorter branched side chains can self-assemble into small nuclei, but no complete and regular spherulites formed. In contrast, the PEODPF film with bulky side chain displayed well-defined spherulite morphology, confirmed by the characteristic birefringence and Maltese Cross under the polarized optical microscope (POM) (Fig. 1c, d and Supplementary Fig. 5a, iv). These observations suggest that the formation of spherulites relies on the introduction of bulky branched side chains, which weakens the aggregation between chains and provides more space for crystal nuclei growth, thereby facilitating the formation of highly ordered spherulites. Furthermore, the prominent crystalline ability of PEODPF is proved by the single crystal structure analysis of monomer (Fig. 1b), where the herringbone molecular packing induced by the branched alkyl chains favors the interchain π - π stacking^{9,23–25}. The results simulated by Material Studio (Supplementary Fig. 5d) predicted that the crystal grows along the a -axis direction of crystal cell, further indicating the tendency of fibrillar crystals to grow along the direction of polymer chain axis. Consistent with the polymer spherulite crystallized from viscous melts and solutions at large undercooling, the PEODPF spherulite formed through the SVA approach also involves two stages: (i) primary nucleation and (ii) crystal growth²⁶. As observed in Fig. 1c, nano-crystal nuclei formed spontaneously in the pristine film during the early stages of growth, acting as primary nucleation sites for the subsequent radial growth of spherulites. Then, the primary spherulites appear as sheaves of fibrillar crystals, resembling fan-shaped bundles, which assemble by the orderly packing of the fluorene backbone. These fibrillar crystals continued to grow outward and branch irregularly around the nucleus. As more nanofibres grow together, the size of the spherulite gradually increases, forming boundaries when neighboring spherulites contact each other. Eventually, the film is covered by spherulites ranging in diameter from a few micrometers to hundreds of micrometers, and the size of spherulite can be easily controlled by tuning the environmental temperature of SVA process (Fig. 1d). We counted the average radius of spherulite in PEODPF film grown at different temperatures, and the largest average radius ($\sim 200 \mu\text{m}$) can be obtained at -50°C , suggesting that this temperature is optimal for the growth of spherulite (Fig. 1e and Supplementary Table 1). Additionally, we studied the influence of different solvents on spherulite growth during the SVA process and found that chloroform is the most effective solvent for promoting spherulite formation (Supplementary Fig. 6). The temperature and solvent dependence of spherulite prove that the growth of fibrillar crystals is closely related to chain activity, and a properly saturated solvent vapor atmosphere provides sufficient time for molecular realignment and assembly into highly

ordered configurations. It is noteworthy that this type of spherulite undergoes heterogeneous nucleation, self-seeded by polymer crystals, as confirmed by the central images (Fig. 2a).

Morphology and structure characterization

The micromorphology of submillimeter-scale spherulites is systematically explored by the atomic force microscope (AFM), scanning electron microscope (SEM), and transmission electron microscope (TEM). The micromorphology of spherulite center displayed in Fig. 2a and Supplementary Fig. 7a, crystal nucleus and the surrounding bundle-like lamellas are observed, which consisted of irregular nanofibres (Fig. 2b and Supplementary Fig. 7b). Spherulite is composed of cylindrical nanofibres aligned orderly, as evidenced by the cross-section SEM image of film (Fig. 2b and Supplementary Fig. 7d). The width of a single nanofibre is about 42 nm, according to the statistical data shown in Fig. 2c. The degree of polymerization of PEODPF is approximately 88, based on the number-average molecular weight (39.3 kDa), and the length of a fluorene unit is 0.83 nm determined from the single crystal data. Combining the values mentioned above, the extended single chain length of PEODPF is estimated to be about 73 nm, which is twice the width of a single nanofibre in PEODPF spherulites. This indicates that the nanofibres are composed of folded chains that align parallel to the nanofibre growth direction (Fig. 2f). The stacking model of submillimeter-scale spherulite is further investigated by high-resolution electron microscopy (HR-TEM) and selected-area electron diffraction (SAED) characterization in Fig. 2d and Supplementary Fig. 7e. The lattice stripe spacing is about 0.24 nm with an excellent periodic interchain arrangement, which could enhance the exciton diffusion length. Meanwhile, the multiple diffraction spots in the SAED pattern image and grazing incidence wide-angle X-ray scattering (GIWAXS) (Fig. 2e) also further confirm the polycrystalline structure of interchain stacking in PEODPF spherulite film. Along the out-of-plane direction, the diffraction peak (100) at q_z of 5.8 and 14.2 nm^{-1} corresponds to the interchain spacing ($d_{100} = 1.08$ and 0.44 nm) in the vertical direction of the edge-on interchain arrangement. Along the in-plane direction, the diffraction peak at 8.8 nm^{-1} ($d_{001} = 0.71 \text{ nm}$) of q_{xy} is attributed to the periodicity of fluorene monomers. Therefore, combining the GIWAXS results, we illustrated the chain stacking model of the spherulite, including the interchain stacking distance (1.09 nm), the characteristic peak of fluorene (0.71 nm), and the π - π interaction distance (0.44 nm), as shown in Fig. 2f. Generally, the degree of interchain packing order is closely associated with the exciton diffusion as mentioned above. Thus, we inferred that the spherulite film with well-aligned nanofibres will provide a remarkably uniform energy landscape, which may benefit the exciton diffusion with a narrowing of the excitonic density of states. Meanwhile, these uniform interchain packing also permits an excellent orientation of polymer chain and may further benefit for its transportation of exciton transition dipole moments^{27,28}.

Photophysical properties

From the absorption spectra of the PEODPF film (Fig. 3a), we observed that the spherulite film (Spherulite) and pristine film (Film) exhibit similar absorption peaks at about 387 nm, attributed to the polyfluorene backbone. Compared with the absorption spectra of Film, Spherulite exhibits a broader spectral profile and a stronger absorption edge at longer wavelength, which could be attributed to their higher order chain packing and the scattered light of their crystalline structure. Raman spectra of spherulite and spin-coated film showed negligible differences, indicating the film crystallization does not alter the backbone planarity of polymer (Supplementary Fig. 8a). Photoluminescence (PL) spectra with fine vibrational structures are observed in Film and Spherulite with peaks both at 434, 462, and 495 nm (0-0, 0-1, and 0-2 vibrational transitions), respectively. Compared to that of the Film, the 0-1 and 0-2 vibrational transitions of the Spherulite are

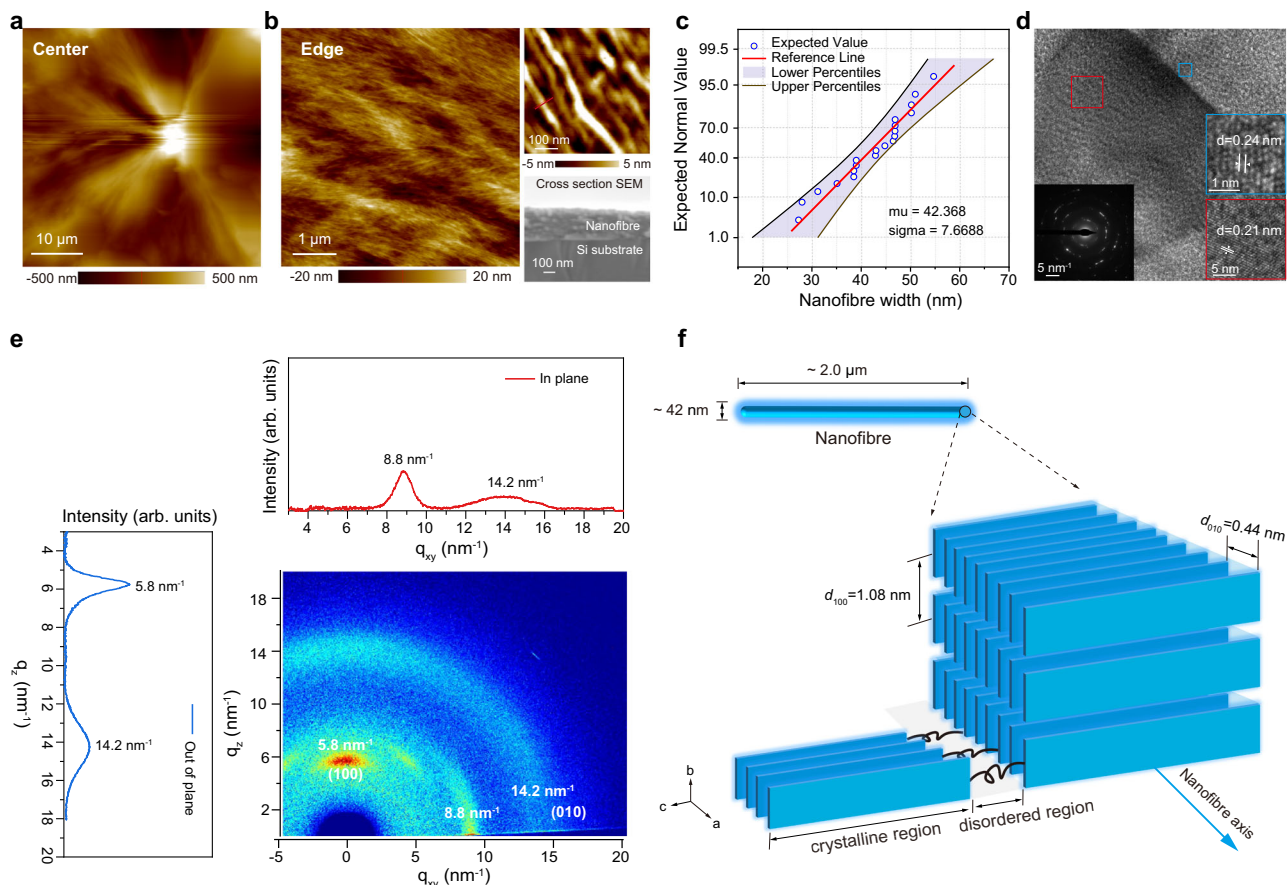


Fig. 2 | Morphology characterization and chain packing of PEODPF submillimeter-scale spherulites. **a** Atomic force microscope (AFM) images of spherulite center. **b** AFM and cross-section scanning electron microscope (SEM) image of spherulite edge. **c** Normal quantile-quantile plot of nanofibres width in spherulites. **d** High-resolution electron microscopy (HR-TEM) image and TEM

selected-area electron diffraction pattern (SAED, lower left) of spherulite. **e** Grazing incidence wide-angle X-ray scattering (GIWAXS) pattern of spherulite film, and out-of-plane (blue line), in-plane (red line) profiles for a plane of incidence. **f** Schematic diagram of the interchain stacking model.

weaker due to the well-ordered chain stacking in the Spherulite. To elucidate the impact of molecular ordering on excitonic behavior, we systematically investigated the radiative and non-radiative recombination dynamics of the spherulite and pristine films. Based on the photoluminescence quantum yield (PLQY, ϕ) and transient PL decay characteristics (τ), the calculated radiative decay rate (k_r) of spherulite film is $7.9 \times 10^8 \text{ s}^{-1}$, higher than that of pristine film, while the non-radiative decay rate (k_{nr}) is $2.2 \times 10^9 \text{ s}^{-1}$, lower than that of pristine film (Fig. 3b and Supplementary Fig. 8b). The excitation energy-dependent PLQY measurements (Fig. 3c) further reveal that the Spherulite exhibits a higher average PLQY ($\sim 40\%$) than the Film ($\sim 30\%$) and remains stable at high excitation energies, suggesting the ordered stacking structures in spherulites can reduce non-radiative energy losses. This improvement is further confirmed by the analysis of the bandgap tail states (E_U) by fitting the photothermal deflection spectroscopy (PDS)²⁹. The E_U value of spherulite film is 48.1 meV, lower than the 52.9 meV of pristine spin-coated film (Fig. 3d), confirming a reduced trap state density. To further trace the ultrafast exciton decay behavior in Spherulite and Film, the fluence-dependent femtosecond-transient absorption (f -TA) measurements were performed under pump fluences of 1.5, 3, 5, 10, and 15 $\mu\text{J cm}^{-2}$ with 400 nm excitation (Supplementary Fig. 9a, c). The differential absorption (ΔA) spectra from 1 to 200 ps exhibit consistent spectral features across fluences (Supplementary Fig. 9b, d), including the ground state bleach (GSB) peaks at 415 nm for Film and 416 nm for Spherulite, along with stimulated emission (SE) signals at 450 nm. These features are similar to the ΔA spectra previously reported for related polyfluorene derivatives^{30,31}. In

Fig. 3e and Supplementary Fig. 10, the normalized SE dynamics are fitted using a tri-exponential function, and the intensity-weighted averaged lifetimes are summarized in Supplementary Table 2. The Spherulite film exhibits a notably longer stimulated emission (SE) lifetime (136 ps) than the amorphous Film (97 ps), suggesting that the ordered molecular packing facilitates exciton diffusion and radiative recombination. Interesting, fluorescence lifetime imaging microscopy (FLIM) reveals that the longer average fluorescence decay time (τ_m) of spherulite film (470 ps) than that Film (360 ps) (Fig. 3f and Supplementary Fig. 11a), supporting that ordered crystalline domains promote rapid exciton transport and delocalization, thereby reducing exciton trapping and enhancing radiative decay rate, in agreement with the observed enhancement in PLQY. Taken together, these results indicate that enhanced molecular order and suppressed defect states in Spherulite contribute to improved excitonic performance and reduced non-radiative losses. Generally, the crystalline film exhibited intriguing optical anisotropy, which may promote exciton diffusion capacity^{28,32,33}. Thus, we further investigated the anisotropic properties of Film and Spherulite through fluorescence anisotropy imaging microscopy (FAIM) images (Fig. 3g, h). The value of fluorescence anisotropy (r) is defined as:

$$r = \frac{I_{//} - I_{\perp}}{I_{//} + 2I_{\perp}} \quad (1)$$

where $I_{//}$ and I_{\perp} represent the fluorescence intensities polarized parallel and perpendicular to the excitation polarization, respectively. The

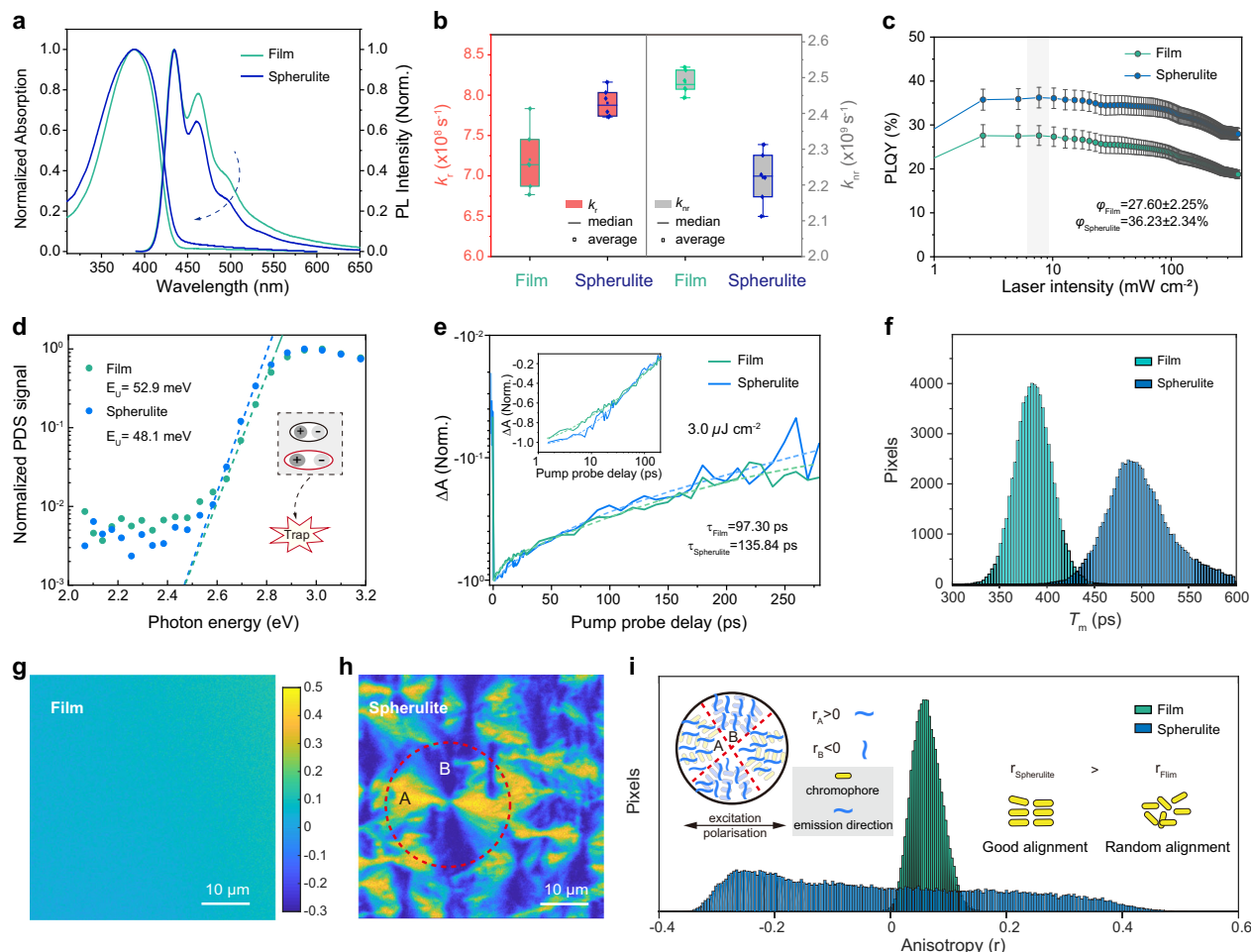


Fig. 3 | Photophysical properties of PEODPF spin-coated and spherulite films. **a** Normalized absorption and photoluminescence spectra of PEODPF spin-coated (Film) (green line) and spherulite films (Spherulite) (blue line). **b** The calculated radiative decay rate (k_r , red) and the non-radiative decay rate (k_{nr} , gray) of the Film and Spherulite (Data were presented as mean values \pm s.d., $n = 6$). **c** Photoluminescence quantum yield (PLQY, ϕ) value of the Film and Spherulite under different excitation energies (Data were presented as mean values \pm s.d., $n = 6$). **d** Photothermal deflection spectroscopy (PDS) curve of Film and Spherulite

(E_U , the bandgap tail states). **e** The differential absorption (ΔA) kinetics of Film (green) and Spherulite (blue) trace at 450 nm with $3.0 \mu\text{J cm}^{-2}$ fluence (typical of the ultrafast decay of stimulated emission). **f** Distribution diagrams for the average fluorescence decay time (τ_m) obtained from fluorescence lifetime imaging microscopy (FLIM). Fluorescence anisotropy images (FAIM) of Film (**g**) and Spherulite (**h**). **i** Fluorescence anisotropy (r) distribution histograms and schematic diagram of emission direction in regions A and B.

value of $r > 0$ indicates emission parallels with the excitation polarization direction, while $r < 0$ means the emission is perpendicular to the excitation polarization direction. As illustrated in Fig. 3i, the pristine film shows uniform r with values ranging from 0 to 0.2, narrower than the spherulite film that ranges from -0.4 to 0.4 . The optical anisotropy is also confirmed by the angle-dependent PL measurement (Supplementary Fig. 11b and Supplementary Fig. 11c). As known, the alignment of chromophores in polymer films significantly affects exciton behavior, energy transfer and luminescence performance, which is crucial for the optoelectronic properties of luminescent polymers³⁴. The higher r value observed in Spherulites suggests its higher ordered chromophores alignment structure, making energy and exciton diffuse easier along the alignment direction. This research indicates that the strong coupling of adjacent chromophores in Spherulite is foreseeable due to their ordered molecular chain packing structure. In addition, their electron energy transfer pathways include intrachain and interchain, with the former involving energy transfer along the backbone between adjacent fluorene conjugated fragments. The latter is achieved through energy hops between spatially coupled chain segments due to the self-folding of molecular chains within the Spherulite. These results demonstrate that the ordered PEODPF chains

in spherulite can substantially improve their luminescence efficiency and excited state lifetime, thereby providing the possibility for obtaining long-range exciton transport.

Exciton diffusion length characterization

To further explore the excitonic behaviors in spherulite, transient photoluminescence microscopy (TPLM) is used to visualize their exciton diffusion property^{35,36}. Supplementary Fig. 12 displays a schematic diagram of the TPLM setup. The principle of this method involves exciting the spherulite and collecting signals to reconstruct the temporal and spatial emission intensity distribution, and exciton diffusion is represented by the expansion of the fluorescence emission intensity distribution over decay time. As shown in Fig. 4a, the diameter of the excitation spot (beam center) irradiated on the nanofiber bundles is about 238 nm, covering several single nanofibers. The TPLM images of spherulite shows the PL intensity distribution along the x-scanning direction as a function of decay time (Fig. 4b). Compared to the TPLM image of a single crystal, the spherulite exciton diffusion state is not very obvious, which could be attributed to the emission signal is collected from a branch of not perfectly horizontally aligned nanofiber bundles (Fig. 4a). As a result, it can increase the energetic

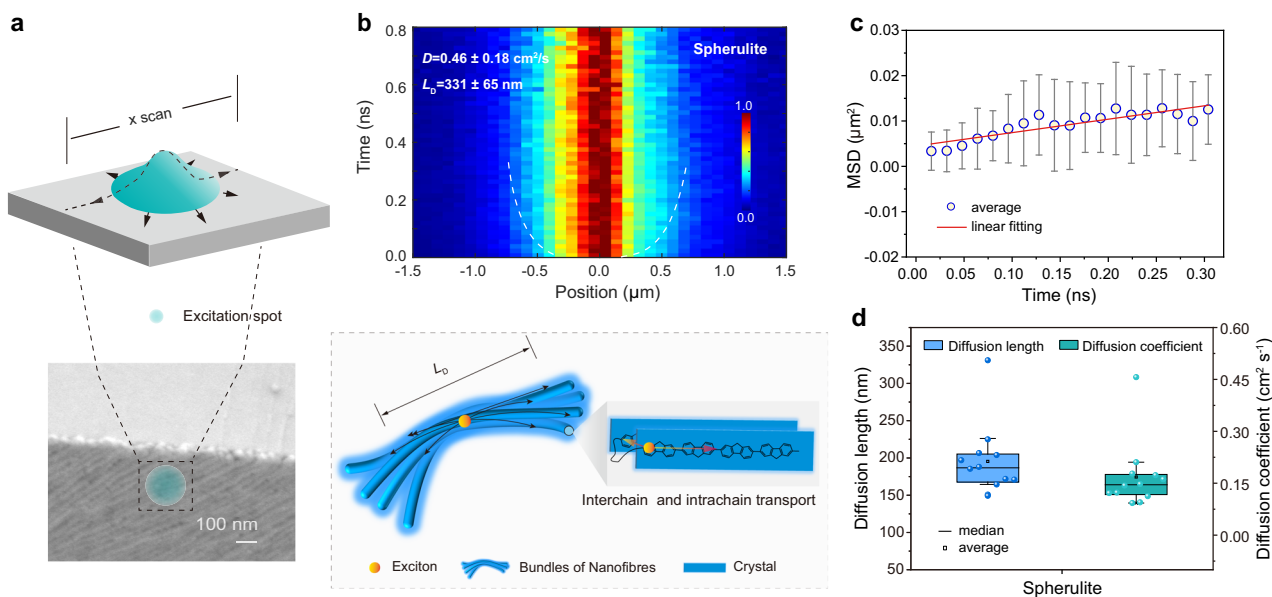


Fig. 4 | Exciton diffusion in PEODPF submillimeter-scale spherulite. **a** Schematic illustrating the route of the exciton transport in submillimeter-scale Spherulite and excitation spot on nanofibres bundles. **b** Normalized transient photoluminescence microscopy (x, t) image to emphasize the exciton diffusion at room temperature.

c Fitting of mean-square-displacement (MSD) of the exciton population from 0 to 0.3 ns (Data were presented as mean values \pm s.d., $n = 12$). **d** Statistical diagram of diffuse coefficient (D) and length (L_D) distribution of bundles nanofibers (Data were presented as mean values \pm s.d., $n = 12$).

disorder and local electronic perturbation, and indistinct exciton diffusion in the TPLM image. For further quantitative analysis, we utilize the mean squared displacement (MSD) model to extract the diffusion coefficient (D) from the slope of the time-related variance of the PL intensity distribution $\sigma_{\text{int}}^2(t)$, according to Eq. (2)³⁷:

$$D = \frac{\sigma_{\text{int}}^2(t) - \sigma_{\text{int}}^2(0)}{2t} \quad (2)$$

Figure 4c shows the time evolution of the singlet exciton MSD in spherulite, which exhibits a good linear relationship in the range of 0–0.3 ns. At longer times $t > 0.3$ ns, exciton–exciton annihilation (EEA) becomes the dominant process, and together with exciton trapping, reduces the spatial spread of the exciton distribution, leading to a decrease in the calculated MSD values (Supplementary Fig. 14). By performing TPLM measurements on various samples, the statistics of D is established and the average D can be reliably fitted as $0.146 \text{ cm}^2 \text{ s}^{-1}$, with the D_{max} of $0.45 \pm 0.18 \text{ cm}^2 \text{ s}^{-1}$ (Fig. 4d, Supplementary Fig. 14, and Supplementary Table 3). Combining with the equation $L_D = \sqrt{2Dt}$, the L_D is calculated to be an average of 186.37 nm with a maximum of 331 ± 65 nm. The maximum value of D is still high for semiconductor polymer films, although reported the bundled nanofibers make the exciton diffusivity lower³⁸. The prolonged exciton diffusion length in spherulites proves that the well-ordered polymer chain packing and less defect structures could assist to slow down the exciton deactivation rate and extend the relative luminescent lifetime, which further favors the enhancement of the emission property and excitonic organic electronic devices efficiency.

PLEDs fabrication and characterization

In order to validate the feasibility of this submillimeter-scale spherulite film on multi-layer optoelectronic devices, we constructed PLEDs with the pristine and spherulite film adopted the structure shown in Fig. 5a (the detailed process is depicted in Supplementary Fig. 15a). PLEDs based on film and spherulite show similar electroluminescence (EL) spectral profile with maximum emission peak (λ_{max}) at 436 and 435 nm (0-0 emission), consistent with their PL spectra (Fig. 5b). Besides, the

corresponding full width at half maximum (FWHM) are calculated about 54 and 43 nm, indicated the small Huang–Rhys factor induced by the weak interchain charge transfer interaction and aggregation in crystalline structures, similar to the PL spectral and TA analysis mentioned above. Therefore, the Commission Internationale de l'éclairage (CIE) chromaticity coordinates also proves better colorimetric purity of Spherulite (0.17, 0.11) than those of device based on spin-coated films (0.17, 0.15) (Fig. 5b and Table 1). In addition, the CIE values of PLEDs based on Spherulite are more stable than those of Film, indicating the slight change in different fabrication batching (Supplementary Fig. 15d). Notably, the Spherulite-based PLED shows an angular dependent EL spectrum that the intensity at 462 nm (0-1) increased with increased angle attributed to their polarized property (Fig. 5c). Due to the fact that the λ_{max} (0-0) of Spherulite-based PLED does not vary with angle, the corresponding angular emission intensity distribution of both devices follows the Lambertian profile (Fig. 5d). As shown in Fig. 5e, the spherulite-based PLED achieve the maximum EQE (EQE_{max}) value of 1.16% and the maximum current efficiency (CE_{max}) of 1.46 cd A^{-1} , which is substantially higher than that of Film-based devices (1.06% and 0.88 cd A^{-1}). According to the EQE equation:

$$\text{EQE} = \text{IQE} \times \eta_{\text{out}} = \gamma \times \eta_r \times \phi \times \eta_{\text{out}} \quad (3)$$

where γ is hole/electron recombination efficiency, η_r is exciton formation probability (0.25 for conventional fluorescent emitters), ϕ is PLQY and η_{out} represents light outcoupling efficiency. When assuming $\gamma = 1$, $\eta_{\text{out}} = 0.2$, $\eta_r = 0.25$, $\phi_{\text{Film}} = 0.3$, $\phi_{\text{Spherulite}} = 0.4$, the theoretical EQE_{max} for the Film and Spherulite devices are calculated to be 1.5 and 2.0%, respectively. The measured values are below these due to an unoptimized device architecture. Nonetheless, the higher EQE in the spherulite-based device correlates with its increased PLQY, indicating reduced non-radiative losses and confirming the key role of molecular ordering in suppressing defect-induced quenching and enhancing overall device performance.

Besides, these devices have a similar turn-on voltage at around 5.3 V, and the maximum luminance (L_{max}) of spherulite-based PLEDs is 4897 cd m^{-2} , much higher (Enhanced by about 47%) than that of Film-based device (3342 cd m^{-2}), as shown in Supplementary Fig. 15b and

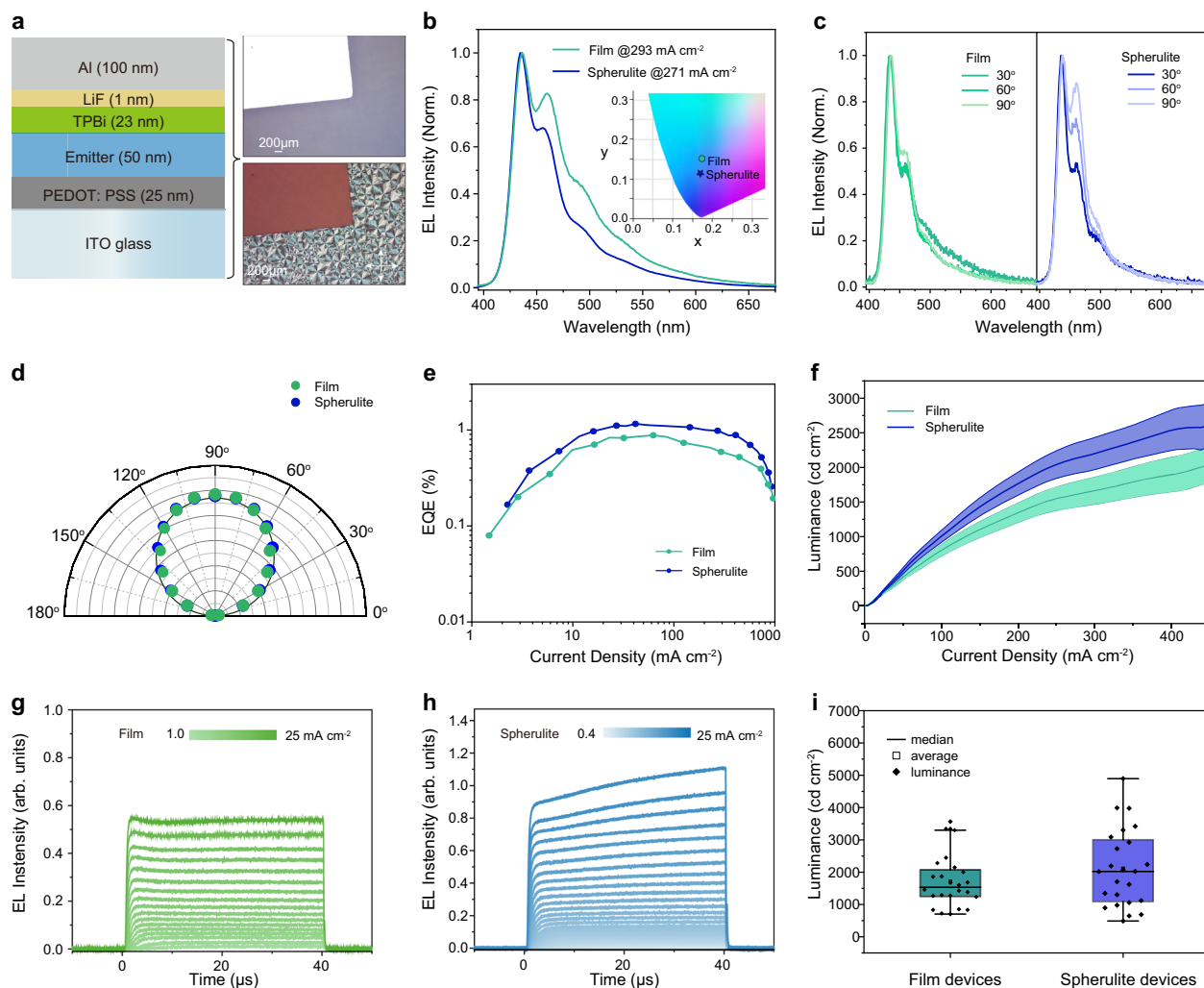


Fig. 5 | Device performance of PLEDs based on PEODPF spherulite and film. **a** Configuration structure of PLEDs and optical image of spherulite emitting layer (top: Bright field, bottom: Polarized light). **b** Electroluminescence (EL) spectra of PLEDs based on film (green) and spherulite (blue) under high current density ($\sim 300 \text{ mA cm}^{-2}$) and corresponding CIE chromaticity coordinates. **c** Angle-dependent EL spectra of Film and Spherulite-based PLEDs. **d** Angular distribution of

emission intensity follows the Lambertian profile. **e** External quantum efficiency (EQE) versus current density curves. **f** Current density versus brightness statistical chart. Transient electroluminescence spectra of PLEDs based on film (**g**) and spherulite (**h**). **i** Statistical diagram of maximum brightness recorded from different PLEDs (Data were presented as mean values \pm s.d., $n = 24$).

Table 1. Then, we counted the L_{max} of two types devices fabricated under the same condition, as shown in Fig. 5i. Apparently, the spherulite-based devices have brightness range of $1000\text{--}4000 \text{ cd m}^{-2}$, relatively higher than the Film-based devices ($1000\text{--}2000 \text{ cd m}^{-2}$). Furthermore, the Spherulite-based PLEDs also display a feature of high brightness at low current density, suggesting that the ordered stacked interchain facilitates carrier transport and increases the carrier concentration (Fig. 5f). The carrier mobility tested by the hole/electron-only carrier devices (Supplementary Fig. 15c) reveals that the excellent electrical properties of submillimeter-scale spherulite film, which also confirms the excellent morphology and dense packing of PEODPF nanofibres to ensure the inter-fiber charge transportation.

To reveal the physical processes of the PLEDs, we study the electronic processes during device operation using transient EL (Tr-EL) analysis³⁹. The typical Tr-EL curves consist of four stages: (i) time delay from pulse voltage turn-on to Tr-EL onset; (ii) EL intensity increased to steady-state value; (iii) stable EL intensity when voltage is on; (iv) EL intensity decay after voltage turns off. In Fig. 5g, the Tr-EL intensity of the Film-based device rises and then reaches stability before showing a

decaying trend with increasing current density (up to 25 mA cm^{-2}) at a pulse duration time of $40 \mu\text{s}$, reflecting exciton–exciton annihilation via singlet–singlet annihilation and singlet–triplet annihilation under high exciton densities, where exciton diffusion is limited and local accumulation becomes significant. Under the same conditions, the EL intensity of the spherulite-based device shows a rising trend with the increase of current density without reaching saturation or decay (Fig. 5h). This behavior is attributed to the low density of the defect structures in spherulite film. Electrons are less prone to defect trapping, which enhances exciton transport and charge mobility, thereby prolonging the recombination process between holes and electrons. Slight enhancement of exciton recombination emission at the plateau state in the Tr-EL curve of Spherulite-based PLED also confirmed the excellent molecular landscape for the transportation of hole and electron injection and transportation, which may reasonably explain their good device efficiency and efficient deep-blue emission. Thus, the ordered stacked interchain arrangement in the spherulite is a feasible strategy to suppress defect formation and exciton utilization rate for achieving high-performance blue light emission.

Table 1 | Device performance of the PLEDs

| Emitter | λ_{\max} [nm] | FWHM [nm] | V_{on} [V] ^a | L_{\max} [cd m ⁻²] | C. E./EQE [cd A ⁻¹ %] _{max} | CIE ^b |
|------------|-----------------------|-----------|----------------------------------|----------------------------------|---|------------------|
| Film | 436 | 54 | 5.4 | 3342 | 1.06 / 0.88 | (0.17, 0.15) |
| Spherulite | 435 | 43 | 5.3 | 4897 | 1.46 (38%)/1.16 (32%) ^c | (0.17, 0.11) |

^aTurn-on voltage at brightness of 1 cd m⁻².

^bCIE coordinate of EL spectra at 300 mA cm⁻².

^cEnhanced efficiency rates are shown in brackets.

Discussion

In summary, large-area submillimeter-scale spherulite films based on branched side-chain modified polydiaryluorene are easily manufactured through an SVA approach. The resulting long-range ordered structure can prolong exciton lifetimes and decrease the density of low-energy state traps. The spherulite film exhibits the highest diffusion coefficient ($\sim 0.63 \text{ cm}^2 \text{ s}^{-1}$) with a long exciton diffusion length (up to 396 nm). Furthermore, the ordered structure contributes to spectral narrowing and improves the color purity of blue emission. Compared to spin-coated films, spherulite-based PLEDs exhibit excellent device performance and high brightness at low current density. Based on our current research, the long-range, well-ordered spherulite structure can significantly improve exciton transport and optoelectronic properties, thereby enriching the materials design strategies for hierarchical π CPs systems and offering a viable platform for investigating supramolecular self-assembly.

Methods

Materials

All reagents and catalysts used in this study were purchased from commercial suppliers and used without further purification unless stated otherwise. 2,2'-bipyridine, 1,5-cyclooctadiene (COD), and bis(1,5-cyclooctadiene)nickel (0) [Ni(COD)₂] were obtained from Sigma-Aldrich. All other drugs used in the synthesis process were obtained from Adamas-beta. Dimethylformamide (DMF) was dried over calcium hydride (CaH₂) and then distilled under a dry nitrogen atmosphere immediately before use. Toluene was dried over sodium (Na) and subsequently distilled under a dry nitrogen atmosphere immediately before use. Anhydrous THF (HPLC grade) was obtained from Solvent Purification Systems (Innovative Technology, Inc.). PEDOT: PSS (Clevios PVP AI 4083) was purchased from Heraeus. The detailed synthesis of PDODPF was provided in the Supplementary Information. The PEODPF, PODPF, and POYDPF used in this paper was synthesized by our previous work.

Preparation of polymer solution, the pristine film (film) and the spherulite film (spherulite)

Polymer solution. The polymer solutions were prepared by dissolving the PEODPF polymer in the chloroform (CF) solvent spontaneously overnight. Various concentrated polymers solution for the spin-coating process is obtained after the heated solution cools to room temperature.

Spin-coated films (Film). Pristine films were spin-casted on quartz or silicon substrates from CF solution (various concentrations) using KW-4A (from the Institute of Micro-electronics of the Chinese Academy of Science) at 1500 for 60 s.

Spherulite films (Spherulite). The spherulite films were prepared by the solvent vapor annealing (SVA) method in Supplementary Fig. 5b. The spin-coated or drop-coated film was placed in a weighing bottle containing chloroform solvent, then the airtight weighing bottle into the oven, setting the oven temperature, and waiting for the chloroform solvent to finish evaporating to get the spherulite film.

Fabrication of polymer light-emitting diodes (PLEDs)

The PLEDs structure is ITO/PEDOT: PSS (50 nm)/EML/TPBi (23 nm)/LiF (1 nm)/Al (100 nm). The detailed fabrication procedure of PLEDs was described as follows. Before spin-coating, the ITO substrate was cleaned in an ultrasonic bath with detergent, acetone, isopropanol and deionized water, dried in an oven at 120 °C for 2 h, and treated with ultraviolet ozone for 10 min. In the spin-coating procedure, a 40 nm thick PEDOT: PSS was firstly spin-coated (Supplementary Fig. 15a, Step 1) and annealed at 120 °C for 20 min (Supplementary Fig. 15a, Step 2). Then, the emitting layer was spin-coated from CF solution (6 mg mL⁻¹) (Supplementary Fig. 15a, Step 3) and the spherulite films were prepared by the SVA method (Supplementary Fig. 15a, Step 4). Next, Film and Spherulite film annealed at 100 °C for 10 min in a nitrogen-filled glovebox. Finally, the other layers, such as 23 nm TPBi, 1 nm LiF and 100 nm Al, were deposited by thermal evaporating sequentially through a shadow mask at a pressure below 1×10^{-5} mbar. The area of the device was 4 mm² defined by the overlap between the ITO and Al electrode. The EL spectra were measured using a QE65 Pro (Ocean Optics) spectrometer in air with encapsulated devices. The structure of single carrier devices ITO/PEDOT: PSS/EML/MoO₃/Al single carrier devices (hole-only) and ITO/ZnO/EML/TPBi/LiF/Al (electron-only) were prepared.

Characterization

General characterization. Nuclear magnetic resonance (NMR) spectra were recorded using a JEOL NMR spectrometer (JNMECZ400S, 400 MHz, Japan), ¹H NMR and ¹³C NMR spectra were referenced to CDCl₃ (¹H NMR: 7.26 ppm, ¹³C NMR: 77.0 ppm). Absorption spectra were measured with a Shimadzu UV-3600 spectrometer at room temperature, and emission spectra were recorded on a Hitachi F-4600 luminescence spectrometer. Nanosecond time-resolved studies were performed with an Edinburgh FLS 980 time-correlated single photon-counting (TCSPC). The transient signal was acquired by TCSPC. Raman microscopy was performed using a Renishaw 2000 CCD spectrometer coupled to an Olympus BH-2 confocal microscope, and using the 633 nm line of a He-Ne laser as the excitation source to avoid absorption and resonance effects. The excitation energy-dependent PLQY of spherulite and pristine film samples were determined by a self-made system by combining a laser (MDL-III-375 nm, spot size is $\approx 0.13 \text{ cm}^2$), an optical fiber, a spectrometer, and an integrating sphere. All films were deposited onto quartz substrates through spin-coating.

Grazing incidence wide-angle X-ray scattering (GIWAXS) test. The GIWAXS measurement was performed at the BL14B1 beamline of the Shanghai Synchrotron Radiation Facility (SSRF) using an X-ray with a wavelength of 1.24 Å. The X-ray beam size was $\approx 0.2 \text{ mm} \times 0.3 \text{ mm}$, as defined by the horizontal and vertical slits.

Film morphology characterization. The polarized optical microscopy (POM) images were performed by NIKON LV100ND. AFM measurement was performed on Park XE-70 atomic force microscopy. Using tapping mode with as little force as possible to collect the topography and phase image of the sample at the same time, the scanning rate was 1 Hz, and the scanning range was 500 nm to 5 μm to obtain the results.

The samples were then examined with a field emission SEM (Hitachi, S-4800) at an accelerating voltage of 5 kV. The transmission electron microscope (TEM) observations were performed with an FEI Talos F 200X microscope operated at 200 kV. (Point resolution 0.25 nm)

Femtosecond-transient absorption (fs-TA) test. Ultrafast TA spectroscopy was conducted using a Ti:sapphire regenerative amplifier (Libra, Coherent Inc.). The second harmonic of the primary beam at 400 nm or an optical parametric amplifier (OperA Solo, Coherent Inc.) pumped by the regenerative amplifier was used to generate the pump beam. The probe beam was a broadband supercontinuum light source generated by focusing a small portion of the femtosecond laser beam onto either a 5-mm-thick CaF₂ plate. The TA signal was then analyzed by a silicon charge-coupled device mounted on a monochromator (Acton 2358, Princeton Instrument) at 1 kHz, enabled by a home-built control board.

Transient photoluminescence microscopies (TPLM) test. Photoexcitation diffusion imaging was performed using a home-built TPLM (Supplementary Fig. 12), a 405 nm picosecond pulsed laser (ALPHALAS) with a repetition rate of 10 MHz and pulse width of 25 ps was focused onto the surface of the sample using an objective lens (Olympus, 100X, Apo, 0.95 numerical aperture). Additionally, the single-photon detecting avalanche photodiode (APD) (SPCM-AQRH, dead time of 28 ns) was used to detect the PL, and the APD was connected to timing electronics (PicoQuant PicoHarp 3000). The measurement of time-resolved PL decay was based on the same excitation light path of the home-built TPLM, but the PL signal was collected by leading it out of the TPLM system through a multimode fiber (Thorlabs, \varnothing 50 μ m, 5 m) with a pair of couplers and collimators (Thorlabs RC08FC-P01) and sending it to another APD (MPD PDM Series 20 μ m) that was also attached to the timing electronics (PicoQuant PicoHarp 300), as shown in Supplementary Fig. 13.

Photothermal deflection spectroscopy (PDS) test. The measurement of PDS was based on NANOPE-PDS-1. The testing scanning range of 350–600 nm. The absorption detection limit of PDS was 0.001%. The thermal deflection solution was 3 M Flourinert.

Transient electroluminescence (Tr-EL) measurement. The Agilent pulse generator (8114 A, 100 V/2 A, rise time <7 ns) is used to provide rectangular pulse voltages (repetition rate: 1 kHz or 100 Hz, pulse width: 3 or 5 μ s) to drive the PLED. Emissions are collected by a Hamamatsu PTM (H10721–20, rise time: 0.57 ns), which is connected to a digital oscilloscope (Agilent DSOX4024A, bandwidth: 200 MHz).

Data availability

The datasets generated during and/or analysed during the current study are available in the Figshare repository, [<https://doi.org/10.6084/m9.figshare.30882692>]. Additional data were available from the corresponding author upon request. The X-ray crystallographic coordinates for structures reported in this study have been deposited at the Cambridge Crystallographic Data Centre (CCDC), under deposition numbers 2521501. These data can be obtained free of charge from The Cambridge Crystallographic Data Centre via www.ccdc.cam.ac.uk/data_request/cif. Source data are provided with this paper.

References

- Lunt, R. R., Giebink, N. C., Belak, A. A., Benziger, J. B. & Forrest, S. R. Exciton diffusion lengths of organic semiconductor thin films measured by spectrally resolved photoluminescence quenching. *J. Appl. Phys.* **105**, 053711 (2009).
- Mikhnenko, O. V. et al. Exciton diffusion length in narrow bandgap polymers. *Energy Environ. Sci.* **5**, 6960 (2012).
- Sajjad, M. T., Ruseckas, A., Jagadamma, L. K., Zhang, Y. & Samuel, I. D. W. Long-range exciton diffusion in non-fullerene acceptors and coarse bulk heterojunctions enable highly efficient organic photovoltaics. *J. Mater. Chem. A* **8**, 15687–15694 (2020).
- Wan, Y., Stradomska, A., Knoester, J. & Huang, L. Direct imaging of exciton transport in tubular porphyrin aggregates by ultrafast microscopy. *J. Am. Chem. Soc.* **139**, 7287–7293 (2017).
- Mikhnenko, O. V., Blom, P. W. M. & Nguyen, T.-Q. Exciton diffusion in organic semiconductors. *Energy Environ. Sci.* **8**, 1867–1888 (2015).
- Jin, X.-H. et al. Long-range exciton transport in conjugated polymer nanofibers prepared by seeded growth. *Science* **360**, 897–900 (2018).
- Sneyd, A. J. et al. Efficient energy transport in an organic semiconductor mediated by transient exciton delocalization. *Sci. Adv.* **7**, eabh4232 (2021).
- Sneyd, A. J., Beljonne, D. & Rao, A. A new frontier in exciton transport: transient delocalization. *J. Phys. Chem. Lett.* **13**, 6820–6830 (2022).
- Khasbaatar, A. et al. From solution to thin film: molecular assembly of π -conjugated systems and impact on (opto)electronic properties. *Chem. Rev.* **123**, 8395–8487 (2023).
- Dimitriev, O. P. Dynamics of excitons in conjugated molecules and organic semiconductor systems. *Chem. Rev.* **122**, 8487–8593 (2022).
- King, A. J. et al. Covalently tethered assemblies improve energetic homogeneity and exciton transport in organic materials. *ACS Mater. Lett.* **6**, 1404–1410 (2024).
- Sánchez-Ruiz, A., Sousa-Hervés, A., Tolosa Barrilero, J., Navarro, A. & Garcia-Martinez, J. C. Aggregation-induced emission properties in fully π -conjugated polymers, dendrimers, and oligomers. *Polymers* **13**, 213 (2021).
- Ma, J., Lu, G., Huang, X. & Feng, C. π -conjugated-polymer-based nanofibers through living crystallization-driven self-assembly: preparation, properties and applications. *Chem. Commun.* **57**, 13259–13274 (2021).
- Lee, J., Kalin, A. J., Yuan, T., Al-Hashimi, M. & Fang, L. Fully conjugated ladder polymers. *Chem. Sci.* **8**, 2503–2521 (2017).
- Han, Y. et al. Diarylfluorene-based organic semiconductor materials toward optoelectronic applications. *Adv. Funct. Mater.* **31**, 2105092 (2021).
- Sun, P., Liu, D., Zhu, F. & Yan, D. An efficient solid-solution crystalline organic light-emitting diode with deep-blue emission. *Nat. Photonics* **17**, 264–272 (2023).
- Pan, Z. et al. Polarization-resolved spectroscopy imaging of grain boundaries and optical excitations in crystalline organic thin films. *Nat. Commun.* **6**, 8201 (2015).
- Shtukenberg, A. G., Punin, Y. O., Gunn, E. & Kahr, B. Spherulites. *Chem. Rev.* **112**, 1805–1838 (2012).
- Ou, C. et al. Hierarchical uniform supramolecular conjugated spherulites with suppression of defect emission. *iScience* **16**, 399–409 (2019).
- Mani, A. & Phani, K. L. N. Spherulitic morphology of electrochemically-deposited poly(paraphenylene) (PPP) films. *J. Electroanal. Chem.* **513**, 126–132 (2001).
- Sun, L. et al. Poly(diarylfluorene) deep-blue polymer light-emitting diodes based on submicrometer-scale morphological films induced by trace β -conformation. *Macromolecules* **55**, 8084–8094 (2022).
- Xu, M. et al. Hierarchical uniform crystalline nanowires of wide bandgap conjugated polymer for light-emitting optoelectronic devices. *Cell Rep. Phys. Sci.* **1**, 100029 (2020).
- Wang, Y. et al. Organic crystalline materials in flexible electronics. *Chem. Soc. Rev.* **48**, 1492–1530 (2019).
- Zhang, X., Dong, H. & Hu, W. Organic semiconductor single crystals for electronics and photonics. *Adv. Mater.* **30**, 1801048 (2018).

25. Ostroverkhova, O. Organic optoelectronic materials: mechanisms and applications. *Chem. Rev.* **116**, 13279–13412 (2016).
26. Crist, B. & Schultz, J. M. Polymer spherulites: a critical review. *Prog. Polym. Sci.* **56**, 1–63 (2016).
27. Cornil, J., Beljonne, D., Calbert, J.-P. & Brédas, J.-L. Interchain interactions in organic π -conjugated materials: impact on electronic structure, optical response, and charge transport. *Adv. Mater.* **13**, 1053–1067 (2001).
28. Müller, K. et al. Directed exciton transport highways in organic semiconductors. *Nat. Commun.* **14**, 5599 (2023).
29. Kronemeijer, A. J. et al. Two-dimensional carrier distribution in top-gate polymer field-effect transistors: Correlation between width of density of localized states and Urbach energy. *Adv. Mater.* **26**, 728–733 (2014).
30. Sun, C. et al. Boosting the stimulated emission properties of host:guest polymer blends by inserting chain twists in the host polymer. *Adv. Funct. Mater.* **32**, 2206723 (2022).
31. Virgili, T. et al. Ultrafast optical gain switch in organic photonic devices. *J. Mater. Chem.* **20**, 519–523 (2010).
32. Sajjad, M. T., Ruseckas, A. & Samuel, I. D. W. Enhancing exciton diffusion length provides new opportunities for organic photovoltaics. *Matter* **3**, 341–354 (2020).
33. Akselrod, G. M. et al. Visualization of exciton transport in ordered and disordered molecular solids. *Nat. Commun.* **5**, 3646 (2014).
34. Xu, Y., Sun, L., Ghiggino, K. P. & Smith, T. A. Resolving conjugated polymer film morphology with polarised transmission and time-resolved emission microscopy. *Methods Appl. Fluoresc.* **12**, 35004 (2024).
35. Zhang, Y. et al. Long exciton diffusion length in high mobility emissive organic semiconductor. *J. Phys. Chem. C* **128**, 3431–3437 (2024).
36. Li, X.-Z. et al. Optical visualization of photoexcitation diffusion in all-inorganic perovskite at high temperature. *J. Phys. Chem. Lett.* **13**, 7645–7652 (2022).
37. Ginsberg, N. S. & Tisdale, W. A. Spatially resolved photogenerated exciton and charge transport in emerging semiconductors. *Annu. Rev. Phys. Chem.* **71**, 1–30 (2020).
38. Wittmann, B. et al. Enhancing long-range energy transport in supramolecular architectures by tailoring coherence properties. *J. Am. Chem. Soc.* **142**, 8323–8330 (2020).
39. Xu, M. et al. A transient-electroluminescence study on perovskite light-emitting diodes. *Appl. Phys. Lett.* **115**, 41102 (2019).

Acknowledgements

W. Huang, J. Lin, X. An, and Y. Han acknowledge support from the Basic Research Program of Jiangsu (BK20243057), the National Natural Science Foundation of China (Nos. 62288102, 22505117, 22105099, 62405134, and 62105262) and the Jiangsu Provincial Senior Talent Program (Dengfeng) (Jiangsu University); L. Sun acknowledge support from the China Postdoctoral Science Foundation under Grant Number 2024M753737 and Shenzhen Science and Technology Program (Grant No. RCBS20231211090610014); X. An acknowledge support from the Natural Science Foundation of Jiangsu Province for Youth (BK20230342); C. Sun acknowledge support from Guangdong Basic and Applied Basic Research Foundation (Grant No. 2024A1515110084) and Guangdong Pearl River Talent Program (Grant No. 2023QN10Z748). We thank Dr. Chujun Zhang from Hunan NanoUp Electronics Technology Co., Ltd for PDS measurements.

Author contributions

L.S. designed and carried out the experiments, wrote this manuscript and Supplementary Materials. Y.Y. and H.F. characterized and simulated exciton diffusion in the spherulite film. Y.X. tested the FLIM and FAIM of spherulite and film. C.W. and Q.Z. characterized the single crystal structure of PEODPF monomer. M.N., Z.Z. and Y.Z. provided assistance with the device preparation. J.W. tested the angular distribution of emission intensity and transient electroluminescence spectra of PLEDs. X.J., C.S., and C.Z. characterized and analyzed the *fs*-TA test of spherulite and film. B.L., Y.Z., and J.C. provided assistance with SEM, TEM, and AFM characterizations. X.A. and L.B. provided assistance in the synthesis of PEODPF and the photophysical properties of the material. M.X. and Y.H. assisted with the analysis of absorption and PL spectra. C.S., L.B., and J.Z. checked and organized the data in the article. J.L. and W.H. initiated this project, provided the crucial idea, and offered enough funds for this work. All authors discussed the results and commented on the manuscript at all stages.

Competing interests

The authors declare no competing interests.

Additional information

Supplementary information The online version contains supplementary material available at <https://doi.org/10.1038/s41467-026-68849-8>.

Correspondence and requests for materials should be addressed to Chen Sun, Lubing Bai, Jinyi Lin or Wei Huang.

Peer review information *Nature Communications* thanks Feng Zhu, and the other, anonymous, reviewer(s) for their contribution to the peer review of this work. A peer review file is available.

Reprints and permissions information is available at <http://www.nature.com/reprints>

Publisher's note Springer Nature remains neutral with regard to jurisdictional claims in published maps and institutional affiliations.

Open Access This article is licensed under a Creative Commons Attribution-NonCommercial-NoDerivatives 4.0 International License, which permits any non-commercial use, sharing, distribution and reproduction in any medium or format, as long as you give appropriate credit to the original author(s) and the source, provide a link to the Creative Commons licence, and indicate if you modified the licensed material. You do not have permission under this licence to share adapted material derived from this article or parts of it. The images or other third party material in this article are included in the article's Creative Commons licence, unless indicated otherwise in a credit line to the material. If material is not included in the article's Creative Commons licence and your intended use is not permitted by statutory regulation or exceeds the permitted use, you will need to obtain permission directly from the copyright holder. To view a copy of this licence, visit <http://creativecommons.org/licenses/by-nc-nd/4.0/>.

© The Author(s) 2026

¹State Key Laboratory of Flexible Electronics (LOFE) & Institute of Advanced Materials (IAM), Nanjing Tech University (NanjingTech), 30 South Puzhu Road, Nanjing, China. ²School of Flexible Electronics (SoFE) & State Key Laboratory of Optoelectronic Materials and Technologies, Sun Yat-sen University, 66 Gongchang Road, Shenzhen, China. ³State Key Laboratory of Precision Measurement Technology and Instruments, Department of Precision Instrument, Tsinghua University, 30 Shuangqing Road, Beijing, China. ⁴School of Chemistry and ARC Center of Excellence in Exciton Science, University of Melbourne, Parkville, VIC, Australia. ⁵State Key Laboratory of Flexible Electronics (LOFE) & Institute of Advanced Materials (IAM), Nanjing University of Posts & Telecommunications (NUPT), 9 Wenyuan Road, Nanjing, China. ⁶National Laboratory of Solid-State Microstructures, School of Physics, and Collaborative Innovation Centre for Advanced Microstructures, Nanjing University, Nanjing, China. ⁷Dongguan Key Laboratory of Micro-Nano Optical Field Manipulation and Sensing, School of Physical Sciences, Great Bay University, Dongguan, China. ⁸Institute of Quantum and Sustainable Technology (IQST), School of Chemistry and Chemical Engineering, Jiangsu University, Zhenjiang, China. ✉e-mail: sunchen@gbu.edu.cn; iamlbbai@njtech.edu.cn; iamjylin@njtech.edu.cn; vc@nwpu.edu.cn